

Suppression of surface recombination in surface plasmon coupling with an InGaN/GaN multiple quantum well sample

Hsiang-Chen Wang,^{1,*} Xuan-Yu Yu,¹ Yu-Lun Chueh,² Tadas Malinauskas,³ Kestutis Jarasiunas,³ Shih-Wei Feng⁴

¹Graduate Institute of Opto-Mechatronics, National Chung Cheng University 168 University Rd., Min-Hsiung, Chia-Yi 62102, Taiwan

²Department of Materials Science and Engineering, National Tsing-Hua University 101, Sec. 2, Kuang-Fu Road, Hsinchu 30013, Taiwan

³Institute of Applied Research, Vilnius University, LT-10222 Vilnius, Lithuania

⁴Department of Applied Physics, National University of Kaohsiung, 700 Kaohsiung University Rd., Nanzih District, Kaohsiung 81148, Taiwan

*hcwang@ccu.edu.tw

Abstract: Temperature-dependent picosecond non-degenerate four-wave-mixing experiments were performed to explore the carrier dynamics in an InGaN/GaN multiple quantum well sample, in which light emission enhancement with surface plasmon (SP) coupling has been identified. In the time-resolved photoluminescence results, we can identify the faster carrier decay time of the sample with surface plasmon coupling. The faster decay time is due to this sample's ability to create additional channels for effective carrier recombination. In the four-wave-mixing results, a slower grating decay time of the sample with surface plasmon coupling was measured. The diffusion coefficients and surface recombination velocities of photo-created carriers were estimated by modeling the decay rate of transient grating signals. For the sample for which surface plasmon coupling exists, smaller diffusion coefficients and slower surface recombination velocities can be estimated when the temperatures are above 150 K. The carriers coupling with some SP modes is not the only mechanism contributing to emission enhancement. In the InGaN/GaN multiple quantum well sample, surface recombination suppressed by SP coupling is another factor for increased light emission efficiency.

© 2011 Optical Society of America

OCIS codes: (160.6000) Semiconductors, including MQW ; (320.7150) Ultrafast spectroscopy.

References and links

1. S. A. Maier, *Plasmonics: Fundamentals and Applications* (Springer, New York, 2007).
2. S. A. Maier and H. A. Atwater, "Localization and guiding of electromagnetic energy in metal/dielectric structures," *J. Appl. Phys.* **98**(1), 011101 (2005).
3. H. L. Chen, J. Y. Wang, W. H. Chuang, Y. W. Kiang, and C. C. Yang, "Characteristics of light emitter coupling with surface plasmons in air/metal/dielectric grating structures," *J. Opt. Soc. Am. B* **26**(5), 923 (2009).
4. V. V. Klimov and D. V. Guzakov, "Strongly localized plasmon oscillations in a cluster of two metallic nanospheres and their influence on spontaneous emission of an atom," *Phys. Rev. B* **75**(2), 024303 (2007).
5. I. Gontijo, M. Boroditsky, E. Yablonovitch, S. Keller, U. K. Mishra, and S. P. DenBaars, "Coupling of InGaN quantum-well photoluminescence to silver surface plasmons," *Phys. Rev. B* **60**(16), 11564–11567 (1999).
6. K. Okamoto, I. Niki, A. Shvarts, Y. Narukawa, T. Mukai, and A. Scherer, "Surface-plasmon-enhanced light emitters based on InGaN quantum wells," *Nat. Mater.* **3**(9), 601–605 (2004).
7. A. Neogi, C.-W. Lee, H. O. Everitt, T. Kuroda, A. Tackeuchi, and E. Yablonovitch, "Enhancement of spontaneous recombination rate in a quantum well by resonant surface plasmon coupling," *Phys. Rev. B* **66**(15), 153305 (2002).
8. J. B. Khurgin and G. Sun, "Enhancement of light absorption in a quantum well by surface plasmon polariton," *Appl. Phys. Lett.* **94**(19), 191106 (2009).
9. K. Jarasiunas, R. Aleksiejunas, T. Malinauskas, V. Gudelis, T. Tamulevicius, S. Tamulevicius, A. Guobiene, A.

- Usikov, V. Dmitriev, and H. J. Gerritsen, "Implementation of diffractive optical element in four-wave mixing scheme for ex situ characterization of hydride vapor phase epitaxy-grown GaN layers," *Rev. Sci. Instrum.* **78**(3), 033901 (2007).
10. H.-C. Wang, S.-W. Feng, T. Malinauskas, K. Jarasiunas, C.-C. Ting, S. Liu, and C.-Y. Tsai, "Carrier dynamics in InGaN/GaN multiple quantum wells based on different polishing processes of sapphire substrate," *Thin Solid Films* **518**(24), 7291–7294 (2010).
 11. W. C. Liu and D. P. Tsai, "Optical tunneling effect of surface plasmon polaritons and localized surface plasmon resonance," *Phys. Rev. B* **65**(15), 155423 (2002).
 12. T. S. Oh, H. Jeong, Y. S. Lee, J. D. Kim, T. H. Seo, H. Kim, A. H. Park, K. J. Lee, and E.-K. Suh, "Coupling of InGaN/GaN multiquantum-wells photoluminescence to surface plasmons in platinum nanocluster," *Appl. Phys. Lett.* **95**(11), 111112 (2009).
 13. D. B. Tran Thoai, R. Zimmermann, M. Grundmann, and D. Bimberg, "Image charges in semiconductor quantum wells: Effect on exciton binding energy," *Phys. Rev. B Condens. Matter* **42**(9), 5906–5909 (1990).
 14. D. M. Yeh, C. F. Huang, C. Y. Chen, Y. C. Lu, and C. C. Yang, "Localized surface plasmon-induced emission enhancement of a green light-emitting diode," *Nanotechnology* **19**(34), 345201 (2008).
 15. H. C. Wang, S. J. Lin, Y. C. Lu, Y. C. Cheng, C. C. Yang, and K. J. Ma, "Carrier relaxation in InGaN/GaN quantum wells with nanometer-scale cluster structures," *Appl. Phys. Lett.* **85**(8), 1371 (2004).
 16. M. Syvajarvi and R. Yakimova, *Wide Band Gap Materials and New Developments* (Research Signpost, 2007).
 17. H. C. Wang, Y. C. Lu, C. Y. Chen, and C. C. Yang, "Carrier capture times of the localized states in an InGaN thin film with indium-rich nanocluster structures," *Appl. Phys. Lett.* **89**(1), 011906 (2006).
 18. S. Nargelas, T. Malinauskas, A. Kadys, E. Dimakis, T. D. Moustakas, and K. Jarašiuūnas, "Nonlinear carrier recombination and transport features in highly excited InN layer," *Phys. Status Solidi., C Curr. Top. Solid State Phys.* **6**(S2), S735–S738 (2009).
 19. T. Malinauskas, K. Jarasiunas, S. Miasojedovas, S. Jursenas, B. Beaumont, and P. Gibart, "Optical monitoring of nonequilibrium carrier lifetime in freestanding GaN by time-resolved four-wave mixing and photoluminescence techniques," *Appl. Phys. Lett.* **88**(20), 202109 (2006).
 20. K. Binder and D. W. Heermann, *Monte Carlo Simulation in Statistical Physics, 2nd edn.* (Springer, Berlin, Heidelberg 1992).
 21. I. Vurgaftman and J. R. Meyer, "Band parameters for nitrogen-containing semiconductors," *J. Appl. Phys.* **94**(6), 3675 (2003).
 22. T. Malinauskas, K. Jarasiunas, M. Heuken, F. Scholz, and P. Bruckner, "Diffusion and recombination of degenerate carrier plasma in GaN," *Phys. Status Solidi., C Curr. Top. Solid State Phys.* **6**(S2), S743–S746 (2009).
-

1. Introduction

Surface plasmons (SP) are the collective oscillation of electrons on a metal/dielectric (semiconductor) interface. Depending on its propagation characteristics, SP can be classified into two categories: surface plasmon polariton (SPP) and localized surface plasmon (LSP) [1]. An SPP can propagate along a continuous metal/dielectric interface or a periodical metal arrangement. A dispersion curve can be drawn for an SPP to demonstrate its propagation speed and densities of states. On the other hand, an LSP oscillates locally on an isolated metal nanoparticle or a metal groove or bump with a fixed oscillation frequency. Normally, its dispersion curve is a straight line, indicating its zero propagation velocity and broad-angle emission and absorption characteristics. The properties of an SPP or LSP depend on the properties of the metal, the metal nano-morphology, the properties of the surrounding dielectric material, and the excitation mechanism [2,3]. Either both SPP and/or LSP extend(s) its/their electromagnetic field(s) (near field) distribution into the surrounding dielectric material for several tens of nm. The coverage of a nearby light emitter (such as a semiconductor material) by the near field of an SP can result in the energy coupling between the SP and the light emitter. The coupling process is similar to the stimulated emission in a laser system and its strength follows Fermi's golden rule [4]. Therefore, the coupling can be very strong and fast, leading to effective energy transfer from a light emitter into an SP mode. Such a coupling process can be used for enhancing the emission efficiency of a light emitter, particularly when the intrinsic emission efficiency is low [3,5–8]. In emission enhancement, the emitter effectively couples its excited energy into an SP before it is consumed by the non-radiative recombination centers, for effective emission if the momenta of the SP and photon can be well matched. In using SP coupling for enhancing LED efficiency or generating certain preferred functions, by preparing a metal structure on the LED top surface, the coupling of an

induced SP with the QWs of the LED results in carrier energy transfer into the SP for emission. In other words, an alternative light emission channel is created besides the radiative recombination of carriers in the QWs. The energy flow in such an SP-QW coupling process shows that besides the nonradiative carrier recombination in the QWs to produce energy loss, the alternative emission channel through SP coupling also produces an alternative loss channel due to metal dissipation of SP energy. Therefore, whether the alternative emission channel is useful for improving the LED efficiency depends on the relative strengths of the two loss channels. For an LED with low-quality QWs of high defect density, the alternative emission channel through SP coupling is useful. For an LED of high-quality QWs, if the metal dissipation is reduced, the alternative emission channel is still useful. Even if the level of metal dissipation is not low, the alternative emission channel can still be used for generating other LED functions, such as the reduction of the droop effect, generation of intrinsically polarized output, enhancement of light extraction, and decrease of junction temperature.

In this study, we report and interpret the observed temperature dependence of carrier dynamics in an InGaN multiple quantum well sample with SP coupling, in which light emission enhancement has been identified from transmission ratio spectrum and PL results. We use a non-degenerate ps four-wave-mixing (FWM) setup to monitor the carrier diffusion process. A FWM scheme with a diffraction optical element as a beam splitter and a ps parametric generator at 420 nm was used to record the transient free-carrier grating in the multiple quantum wells (MQWs) and avoid optical absorption by the GaN layers. The carriers were generated in a submicron-thick surface layer and their dynamics were monitored by the delayed probe beam at wavelength (λ) = 1064 nm. The period of transient grating was changed in a range from 3 to 7 μm by varying the angle θ , thus providing a unique advantage to measure in-plane carrier diffusion and lifetime. The temperature in the time-resolved FWM experiments was varied using a closed-cycle He-gas cryostat.

This paper is organized as follows: In Section 2, the sample preparation, characterization, and optical measurements are presented. The implementation of the time resolved FWM scheme is reported in Section 3. Section 4, then discusses all the spectroscopy results, and also modeling of nonequilibrium carrier dynamics are given. Finally, the conclusions are drawn in Section 5.

2. Sample preparation and optical measurements

The InGaN/GaN MQW structures were grown by metalorganic chemical vapor deposition (MOCVD) on a c-plane sapphire substrate. The epitaxial structure consisted of a low temperature GaN nucleation layer, a 3 μm thick GaN epilayer, five pairs of InGaN/GaN MQWs, and a 10 nm thick GaN cap layer. For MQWs, the well and the barrier, with thicknesses of 3 nm and 10 nm respectively, were deposited, leading to an emission wavelength around 490 nm. Such a sample is called the bare MQW sample. The other sample, called the Ag-coated sample, is produced by 60 min of thermal annealing at 200°C, followed by a 10 nm-thickness Ag coating on the top of a bare MQW sample. Both the PL and TRPL (Time-Resolved Photoluminescence) measurements were excited by the second harmonic of a femtosecond Ti:Sapphire laser at 790 nm. The excitation and PL signal collection were performed from the polished backside of the sample. The TRPL profiles were recorded with a streak camera of 30 ps temporal resolution. The picosecond non-degenerate FWM technique has been demonstrated in InGaN green emission samples [9,10].

Figure 1 shows the scanning electron microscopy (SEM) image of the metal surface of the Ag-coated sample. Figure 2(a) shows a 0.75 μm \times 0.75 μm atomic-force microscopy (AFM) image of the same sample. Figure 2(b) shows a line-scan profile in an AFM measurement of the same sample along the straight line in Fig. 2(a). One can see that after thermal annealing of the Ag-coated sample, the Ag nanocrystals become aggregated to form nanodots of 80-100 nm in width and 15-20 nm in height. This result implies that Ag was coated in a morphology similar to nanoparticles. The existence of LSP in a nanograting structure has been numerically

predicated, with the LSP resonance energies higher than those of SPP [11]. Therefore, the LSP modes can exist in the Ag-coated sample with a rough surface.

Figure 3(a) shows the PL spectra of the bare MQW sample and Ag-coated sample at room temperature. One can see that with Ag-coating, the PL intensity is about three times that of the bare MQW sample and the PL peak shows a blue-shift compared with the bare MQW sample.

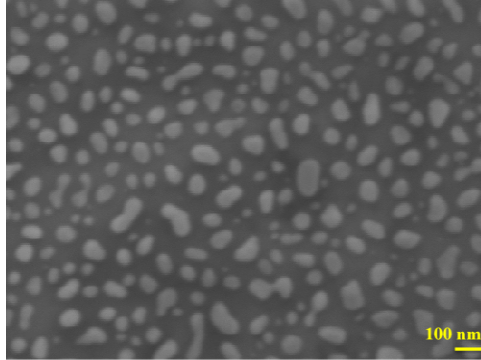


Fig. 1. An SEM image of the 10 nm Ag coating on the top of the bare MQW sample after 60 min of thermal annealing at 200°C.

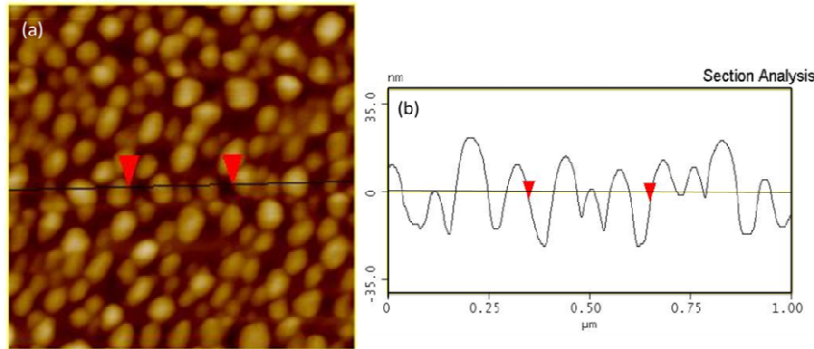


Fig. 2. (a) An AFM image of the Ag-coated sample. (b) An AFM line-scan profile of the Ag-coated sample.

The blue-shift of the PL spectrum indicates one of the important features proving the existence of the MQW-SP coupling process [12]. Electrostatic image charge can also lead to such a blue shift due to the Coulomb interaction change and therefore influence the exciton binding energy in quantum wells [13]. But the material radiation enhancement cannot be achieved by this image charge. Figure 3(a) also shows the transmission ratio spectrum of the two samples. The transmission ratio is the transmission spectrum of the Ag-coated sample divided by the transmission spectrum of the bare MQW sample. In the transmission ratio spectrum, a broad transmission dip is observed, indicating the absorption of LSPs generated on the Ag nanostructures. Because of the large varieties of size and shape of the nanostructures, different LSP modes of different resonance energies lead to the broad transmission dip in Fig. 3(a) [14]. Figure 3(b) shows the temperature-dependent PL peak positions of the two samples. For both samples, the typical S-shape variation can be seen, indicating the existence of composition fluctuations in the MQWs [15]. The Ag-coated sample and the bare MQW sample come from different part of the same one wafer that has the same growth conditions. The PL emission of the Ag-coated sample redshifts from the bare MQW sample due to the slightly non-uniformity of material growth. The magnitude of this redshift is relatively small (about 15 nm). The presence of a temperature dependence of the redshift indicates MQW-SP coupling. The two curves of PL peak are essentially parallel below 180 K.

Beyond that, the PL spectral feature of the Ag-coated sample is rapidly blueshifted as the temperature increases. The blueshift is attributed to the stronger coupling between the carriers and the LSP modes for higher temperatures. For effective SP-MQW coupling, the momentum mismatch between SP and carrier can be easily overcome by thermal activation at temperatures above several tens of Kelvins. However, when the carriers are trapped in potential minima, the coupling efficiency can be significantly decreased although their wave functions include spatial-frequency components that would allow matching of SP and carrier momenta. We are assuming that the wave number of SP, k_{SP} , is three times larger than that of a photon, i.e., $k_{SP} \sim 3(2\pi n/\lambda) \sim 0.1 \text{ nm}^{-1}$. Here, n is the refractive index of GaN (2.5) and λ is the photon wavelength ($\sim 420 \text{ nm}$). For an electron to have such a wave number, it requires a temperature of only $T = \hbar^2 k_{SP}^2 / (2m_e k_B) \sim 50 \text{ K}$ and even lower for a hole. Here, \hbar is the Planck constant divided by 2π , m_e is the electron effective mass in InGaN, and k_B is the Boltzmann constant. Hence, sufficient momentum can be easily obtained for free carriers. However, for a trapped carrier, only a fraction of spatial-frequency components can satisfy such a momentum mismatch. Assuming that a trapped carrier has a Gaussian shaped wave function with 5 nm in width (standard deviation), we can evaluate the mean value and standard deviation of the wave function in the k space to be around 0 and 0.1 nm^{-1} , respectively. The probability of finding a carrier with the wave number larger than 0.1 nm^{-1} is less than 0.5 in a two-dimensional structure. Hence, at a certain temperature, although a pair of trapped carriers can couple with a SP mode, its probability is significantly lower than that of a pair of free carriers. In other words, the delocalization of carriers with increasing temperature can enhance the SP-MQW coupling rate. Nevertheless, the increasing coupling rate cannot be completely attributed to the delocalization process; other possibilities, such as the increase of the SP density of state with temperature, must also be considered.

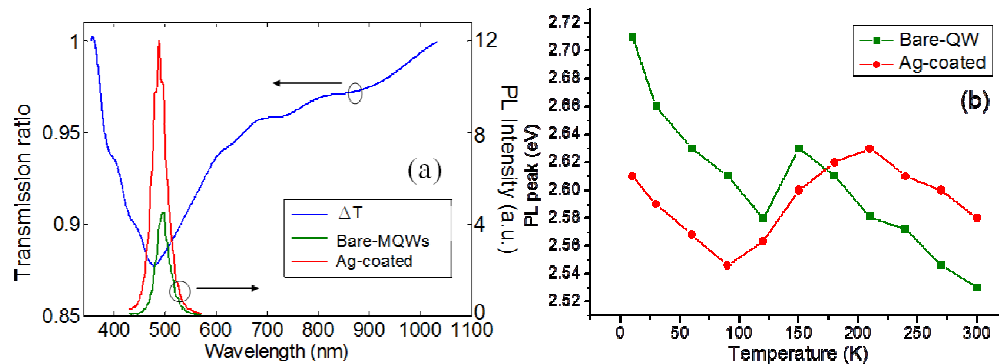


Fig. 3. (a) Room temperature PL spectra (right ordinate) of the two samples showing their relative intensities. Transmission ratio spectrum of the samples (left ordinate). (b) Temperature-dependent PL peak position of the bare MQW sample (green square) and Ag-coated sample (red circle).

3. Time resolved FWM scheme

Time-Resolved Four-Wave Mixing (FWM) experiments were carried out using the setup shown in Fig. 4. Measurements of a wide range of materials require different wavelengths for carrier photoexcitation, therefore various harmonics of a mode locked picosecond YAG:Nd laser (model PL2143 of Ekspla Co.) or an optical parametric generator (model PG401 of Ekspla Co.) were used as light sources. The setup provides pump wavelengths of 532, 355, and 266 nm with pulse energies of 15, 10, and 5 mJ, correspondingly. The initial beam diameter was collimated to 1-2 mm size and used for the grating recording. The parametric generator was tunable in the spectral ranges of 420-680 nm and 740-2000 nm, with maximum pulse energy of about 1 mJ at $\sim 500 \text{ nm}$. In this study, the first harmonic of the laser at 1064

nm was used as a probe beam in most experiments, ensuring the highest sensitivity to the nonresonant refractive index modulation by free carriers. A ps parametric generator at 420 nm as a pump beam was used to record the transient free-carrier grating in the multiple quantum wells (MQWs) and avoid optical absorption by the GaN layers. The pulse energy of the recording beams was attenuated by rotating a $\lambda/2$ plate positioned before the Glan-prism. The difference in optical paths of the interfering beams was adjusted by a short stepper-motor driven pump-delay line that allowed the delay time to vary up to 1.5 ns. Energy of the incident beams was measured by an energy meter, while the beam spatial profile was controlled by a CCD-line. The grating decay kinetics were measured by performing five measurements at a fixed probe beam delay time Δt and integrating the data in a required intensity window of $I_0 \pm \Delta I_0$ (usually $\Delta I_0/I_0 < 5\%$). Exposure characteristics were measured by collecting 500-1000 laser shots at different excitation energies. A data acquisition system based on the Labview software monitored the experiment, processed the data, and presented the measured FWM characteristic in real time. We used the holographic beam splitters (HBS) to split pump beam as two beams to form a dynamic grating in the sample. A simple temporal and spatial adjustment of two interfering beams created by the HBS and easy change of the dynamic grating period (by replacing only the HBS with another grating of a different spacing) makes the novel FWM tool user-friendly, reproducible, and simple in operation. The experimental set-up is shown in Fig. 4. Θ is the angle between two incident beams of the pump beam. A reference paper [9] shows more details about this non-degenerate ps four-wave-mixing by using HBS component. The free-carrier grating through excitation of a crystal with light interference patterns has a number of advantages over other “excite-probe” techniques. These advantages arise due to temporal and spatial modulation of optical properties of a matter by incident light $I(x) = I_0 [1 + \cos(Kx)]$, which generates a spatially modulated nonequilibrium carrier distribution $N(x,t) = N_0(t) + \Delta N(x,t) \cos(Kx)$; here N_0 and ΔN are the nonmodulated and modulated carrier densities along the grating vector $K = 2\pi/\Lambda$ with period Λ . The instantaneous modulation of the electric properties is duplicated by the refractive index n modulation by value $\Delta n(x,t) \sim \Delta N(x,t)$, thus creating a free carrier grating [16]. The decay time of the grating efficiency $\eta(t) \sim \exp(-2\Delta t/\tau_G)$ corresponds to the time interval of the probe beam $\Delta t = \tau_G$ in which the η value decreases by e^2 , while carrier modulation decreases by e in that interval. The similar procure is repeated at some other grating periods, and the corresponding values of τ_G are determined. The plot of the inverse grating decay time $1/\tau_G$ vs. $(2\pi/\Lambda)^2$ (or so called “angular” dependence of decay time) allows determination of the diffusion coefficient as well as the carrier recombination time, as one of them is dependent on grating period:

$$\frac{1}{\tau_G} = \frac{1}{\tau_R} + \frac{1}{\tau_D} \quad (1)$$

Where $1/\tau_R$ is the recombination time and $\tau_D = \Lambda^2/(4\pi^2 D)$ is the diffusion time of the grating erasure.

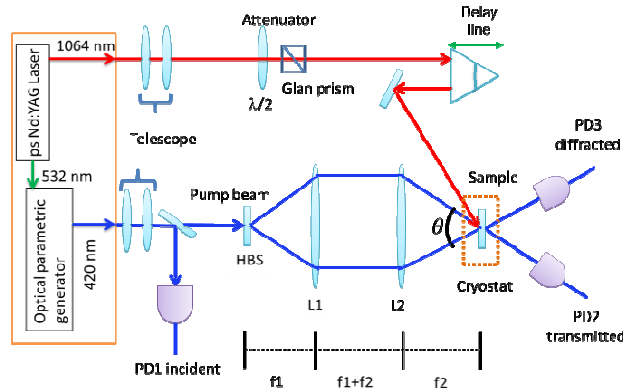


Fig. 4. Optical scheme of nondegenerate four-wave mixing with HBS as the beam splitter.

4. Time-resolved optical measurement and simulation results

To clearly investigate the coupling dynamics between excitons of the MQWs and the SPs of Ag nano-particles, temperature-dependent TRPL and FWM measurements were performed. In order to identify the significant differences between the bare MQW and Ag-coated samples, we show the decay profiles of the two kinds of measurements only at the room temperature. Figure 5(a) shows the TRPL decay profiles of the two samples at room temperature. The more fluctuating green and red lines represent the measured results of the bare MQW and Ag-coated samples, respectively. The smooth lines represent the results of fitting. They show a faster decay profile for the Ag-coated sample than for the bare MQW sample. This is because, when the plasmon mode of the Ag nano-particles is coupled to MQWs, they allow scattering due to the momentum relaxation of SPs and thus couple to the radiated light, resulting in this spontaneous emission rate much faster than that of the bare MQW sample [12]. Figure 5(b) shows the FWM decay profiles of the two samples at room temperature. For both samples, the double-exponential decay traces describe nonlinear processes in the InGaN MQWs and can be attributed to the radiative bimolecular recombination of carriers in InGaN [16]. With such fitting, the fast- and slow-decay times were obtained, as plotted in Fig. 5 (b). One can see that in both temporal traces, after the pump pulse, decay traces with time first quite fast in the several tens of ps range, followed by a slower range from several hundred ps to 1 ns. Traces in Fig. 5 (b) show the temperature-independent variations of the fast decay speed. For the slow-decay traces, the FWM measurements show the opposite result compared to the TRPL measurements. In the FWM measurements, the Ag-coated sample showed a slower decay profile than the bare MQW sample. That means plasmon mode coupling to MQWs will suppress the exciton diffusion to defects, thus decreasing the rate of non-radiative recombination.

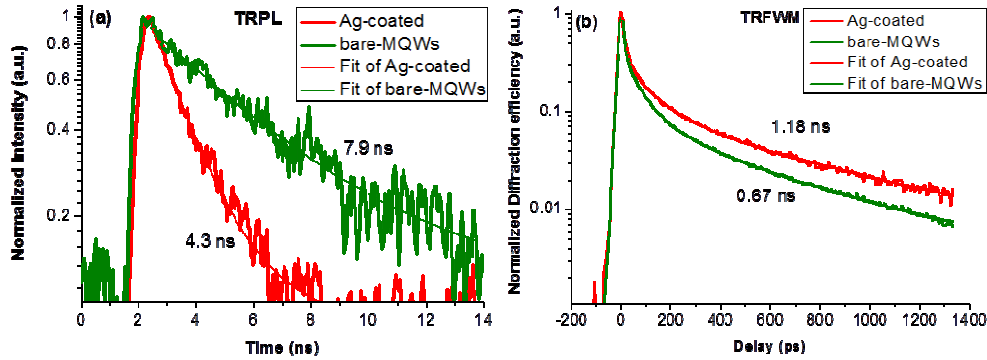


Fig. 5. (a) Time-resolved PL decay profiles of the two samples at room temperature. (b) Time-resolved FWM decay profiles of the two samples at room temperature.

Figure 6 summarizes the temperature-dependent carrier lifetimes on the left ordinate from TRPL measurements and furthermore grating decay times (the decay time of grating efficiency) on the right ordinate from FWM measurements. In the TRPL results, for both samples, at lower temperatures ($T < 60\text{K}$), carrier lifetimes are only slightly changed due to excitons being more localized in indium-rich cluster like energy distribution [17]; at higher temperatures ($90\text{K} < T < 240\text{K}$), the carrier lifetime decreases with temperature meaning excitons are delocalized by thermal energy and nonradiative recombination processes are activated. Meanwhile, the carrier lifetimes of the Ag-coated sample were shorter than those of the bare MQW sample because the existence of MQW-SP coupling creates another channel for effective radiative recombination. Beyond 120K , the differences of carrier lifetimes between two samples became larger due to the MQW-SP coupling rate (i.e., the SP density of state) increasing with temperature. In the FWM results, the temperature-dependent grating decay times of both samples show a similar S-shape variation as the temperature-dependent PL results in Fig. 3(b). This is explained by Fig. 5(b), in which the double-exponential decay traces describe nonlinear processes in the InGaN MQWs. The Auger recombination could be one of the major factors in the FWM measurements [18]. It shows the exciton number will affect the temperature-dependent grating decay time. In the temperature range of about 90K in Fig. 3(b), both samples have lower bandgap energies that will generate more excitons after laser excitement. Auger recombination, dominated by increasing numbers of excitons, caused the faster grating decay times for non-radiative recombination in Fig. 6. In the temperature range about 210K , it shows the opposite result. For comparison with the grating decay times between the Ag-coated sample and the bare MQW sample, the Ag-coated sample, i.e., the SP coupling sample, had longer grating decay times. That means the existence of MQW-SP coupling will suppress carrier diffusion for non-radiative recombination. Beyond 120K , the differences of grating decay times between two samples show the same tendency as the TRPL measurements, i.e., the differences between them increase. Through a combination of TRPL and FWM results in Fig. 6, it can be observed that the carrier lifetimes and grating decay time become closer at higher temperature. This phenomenon indicates that the diffusion coefficient (D) is decreasing with increasing temperature, especially for the Ag-coated sample (solid red line and dashed red line in Fig. 6) [19].

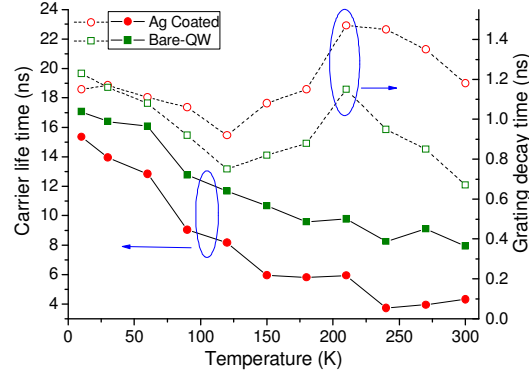


Fig. 6. Carrier lifetime (left ordinate) and grating decay time (right ordinate) as functions of temperature for TRPL and FWM measurements, respectively.

In order to investigate the mechanics of the slower decay times with the Ag-coated sample in the FWM measurements, we calculated the D values of both samples as a function of temperature through fitting various grating periods of FWM results. This paper's hypothesis is that the existence of MQW-SP coupling in the Ag-coated sample increases the emission efficiency by both carrier coupling with SP-modes and also suppression of the surface recombination in the interfaces between barrier layers and quantum wells. The temperature dependence of the surface recombination velocity was calculated using the Monte Carlo simulation [20]. The material parameters used in this calculation are band gap (2.531 eV), electron effective mass ($0.17m_0$, m_e), hole effective mass ($1.94m_0$, m_h), optical phonon energy (91 meV), relative static dielectric constant (10.4), and relative optical dielectric constant (8.9) [21]. The quantitative relationships of the measured light diffraction characteristics with carrier plasma parameters are based on spatial and temporal carrier distributions, dependent on generation, recombination, and transport processes. Therefore, different sets of material equations, depending on excitation conditions, are used to calculate the nonequilibrium carrier dynamics. At grating recording by strongly absorbed beams with quantum energy above the E_g , two-dimensional continuity Eq. (2) is used to calculate the instantaneous carrier profiles $N(x,z,t)$, governed by carrier diffusion along the grating vector x and to the sample depth z , as well as by carrier recombination at the surface and in the bulk:

$$\frac{\partial N(x,z,t)}{\partial t} = \nabla [D(N)\nabla N(x,z,t)] - AN(x,z,t) - BN^2(x,z,t) - CN^3 + G(x,z,t) \quad (2)$$

Here, the boundary conditions for a semi-infinite media or a layer of thickness d are:

$$\left. \frac{\partial N(x,z,t)}{\partial t} \right|_{z=0} = \frac{S_1}{D(N)} N(x,0,t) \quad (3)$$

$$N(x,\infty,t) = 0 \quad (4)$$

$$\left. \frac{\partial N(x,z,t)}{\partial z} \right|_{z=d} = \frac{S_2}{D(N)} N(x,d,t) \quad (5)$$

Here $G(x,z,t) \sim \alpha I(x,z,t)$ is the carrier generation rate by the light interference field, D is the diffusion coefficient, $S_{1,2}$ are the surface recombination velocities, and A , B , C are the coefficients of linear, bimolecular, and Auger recombination. The solution of Eq. (2) provides the spatial and temporal carrier distribution $N(x,z,t)$ which is used to calculate the instantaneous refractive index modulation Δn and diffraction efficiency η :

$$\eta(t) = \left(\int_0^d \frac{\pi \Delta n(z,t) dz}{\lambda} \right)^2 \approx \left(\frac{\pi \Delta n d_{eff}}{\lambda} \right)^2 = \left(\frac{\pi n_{en} \Delta N d_{eff}}{\lambda} \right)^2 \quad (6)$$

We performed the Monte Carlo calculations using the described model and estimated the effective depth that contributes to the FWM signal. Figure 7 shows the carrier diffusion coefficient (left ordinate) and surface recombination velocity (right ordinate) as functions of temperature from FWM measurements and Monte Carlo calculations, respectively. For the temperature dependence of the carrier diffusion coefficient, the D values increase with decreasing temperature due to carrier degeneracy [22]. When the temperature was above 150K, the D values of the Ag-coated sample were lower than those of the bare MQW sample, meaning the MQW-SP coupling activated in the higher temperature range was the same trend as described above. For both samples, the temperature-dependent surface recombination velocity (S) increased with increasing temperature, indicating that carriers with higher thermal energy undergo the more non-radiative recombination with in-plane defects. At temperature above 180K, the S values of the Ag-coated sample are slower than those of the bare MQW sample, meaning excitons were constrained from surface recombination by the SP-modes.

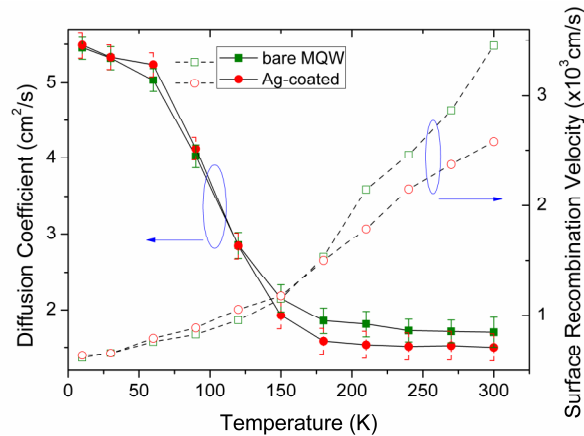


Fig. 7. Carrier diffusion coefficient (left ordinate) and surface recombination velocity (right ordinate) as functions of temperature from FWM measurements and Monte Carlo calculations, respectively.

5. Conclusions

We have used temperature-dependent TRPL and FWM measurements for studying the carrier dynamics in InGaN/GaN multiple quantum well samples, in which MQW-SP coupling has been identified. In particular, we extracted the carrier lifetimes, grating decay times, carrier diffusion coefficients, and surface recombination velocities of both samples as functions of temperature. In the temperature-dependent TRPL measurements, the sample with SP-mode coupling had faster decay traces than the bare MQW sample. In the temperature-dependent FWM measurements, the decay traces show the opposite trend to the TRPL results. Beyond 150 K, the sample with SP-mode coupling had the lower carrier diffusion coefficients and slower surface recombination velocities, indicated that carriers can be bound by SP fields. The emission efficiency increase with SP coupling is due not only to carriers coupling with SP-modes but also to carriers binding with SP fields, thus decreasing surface recombination.

Acknowledgement:

This research was supported by the National Science Council, The Republic of China, under Grant Nos. NSC 99-2221-E-194-020, NSC 98-2112-M-007-025-MY3, NSC 99-2112-M-390-002-MY3, and European Commission Contract No. MRTN-CT-2006-035735.